ERS tandem INSAR processing for DEM generation, glacier motion estimation and coherence analysis on Svalbard

K. ELDHUSET†, P.H. ANDERSEN†‡, S. HAUGE†, E. ISAKSSON‖, D. J. WEYDAHL †

† Norwegian Defence Research Establishment (FFI), Division for Electronics, P.O. Box 25, NO–2027 Kjeller, Norway

‡ University of Oslo (UiO), P.O. Box 1032 Blindern, NO–0315 Oslo, Norway

‖ Norwegian Polar Institute (NPI), P.O. Box 399, Polar Environmental Centre, NO–9296 Tromsø, Norway

Abstract. This paper describes the unique INSAR (Interferometric Synthetic Aperture Radar) processing algorithms at FFI and how ERS tandem data are used to prove the high performance of processing chain. The INSAR baselines are estimated from the high precision orbit data only, without using ground control points in the Svalbard test area. The flattening of the interferograms is of high quality and the interferograms are used to generate INSAR DEM (Digital Elevation Model) by using an existing DEM from Svalbard. The RMS of the INSAR DEM is between 10 and 20 m in the selected test area. Although one–day interferograms with removed terrain fringes were used, a combination of field measurements, photogrammetric methods and interferometry are necessary to obtain a complete pattern of ice velocities on a fast–moving glacier like Kronebreen (maximum 2 m/day), where parts of the glacier are heavily crevassed. The study also demonstrated that considerable decorrelation may occur during 1 day over snow and glaciers due to changing weather conditions.

1. Introduction

1.1 *Background*

Spaceborne synthetic aperture radar interferometry (INSAR) was for the first time published by Goldstein *et al.* (1988) using data from the SEASAT L–band SAR. They combined the complex data from two scenes three days apart over the same region in Cottonball Basin of Death Valley. There were quite few INSAR publications using SEASAT data, however, since the launch of the C–band ERS–1 SAR (1991) numerous papers have been published. The review article by Gens *et al.* (1996) gives a historical review and a brief introduction to INSAR techniques and applications. Many of the publications deal with 3 day interferometry with applications such as topographic mapping, change detection, volcanic hazards, seismic events and glacier flow. The launch of ERS–2 (1995) increased the potentials of interferometric applications since data sets acquired only one day apart became available.

During later years FFI has demonstrated in–house capabilities in key topics for SAR interferometry such as precision SAR processing and interferogram generation, high precision orbit determination and SAR simulation. The ERS tandem mission provided a unique possibility for testing the limitations of spaceborne multi–pass INSAR and demonstration of possible applications. Svalbard was selected by FFI and NPI as test area for that purpose and is one of the most northern populated areas in the world. The two selected test areas are shown in figure 1. The low atmospheric humidity, mountain terrain, sparse vegetation and active glaciers make this

Dette er en postprint-versjon / This is a postprint version.
DOI til publisert versjon / DOI to published version: 10.1080/01431160210153039

area very interesting for SAR interferometry. In addition, NPI had a new digital elevation model (DEM) for Svalbard available and also glaciology expertice which were very useful in this INSAR study. An European Space Agency (ESA) Announcement of Opportunity project was started in 1996 by FFI, NPI and UiO and this paper gives a description of some of the techniques used in the processing of ERS tandem (ERS–1/ERS–2) raw data with applications to DEM generation, glacier motion estimation and coherence analysis.

1.2 *Objectives*

Most users in interferometry do not have control over the precise orbit computation and the SAR processor in an INSAR processor chain. They start with single look complex (SLC) data and precision orbit data (PRC) from the ESA. This paper covers all topics in the processing from raw data and also the interpretation of the geophysical measurements. The objectives in this work is to develop alternative techniques in the INSAR processor chain which may be more accurate or more effective than existing techniques and take the most important applications to prove the high quality of the total INSAR processing chain. It was also important to investigate the accuracy of INSAR DEM generation without using ground control points. A glacier with very complicated motion was selected to challenge the INSAR technique, since only glaciers with relatively smooth motion are usually published. The ERS tandem data set were unique for this purpose. The INSAR processing chain will be described in a rather superficial way, however, the new approaches will be emphasized in each section. In section 2 the FFI INSAR processor is described, as well as the EETF2 SAR processing algorithm, precise orbit determination with GEOSAT, baseline estimation and interferogram generation. In section 3 the DEM generation using an INSAR simulator is described and asessed. In section 4 the ice velcity estimation on the Kronebreen glacier on Svalbard is done and in section 5 a time series of coherence is considered as a function of weather and ground conditions.

2. The FFI INSAR processor

2.1. *EETF2 SAR processing algorithm*

The core of the SAR processing algorithm has been developed by the main author and is based on the two–dimensional exact transfer function (ETF). The two–dimensional point target response in frequency domain (2nd order ETF) can be written (Chang 1992 or Eldhuset 1995)

$$H(\omega_a, \omega_r, R) = \Phi(\omega_r) \exp\left\{ j \left(\frac{A^2}{4B} \right) \right\} \tag{1}$$

where $\Phi(\omega_r)$ is the Fourier transform of the emitted chirp (the down link replica can be used), ω_r is the range frequency and A and B are given by

$$A = a_1 \lambda \left(\frac{2\pi}{\lambda} - \frac{\omega_r}{c} \right) + \omega_a \tag{2}$$

$$B = \frac{1}{2} a_2 \lambda \left(\frac{2\pi}{\lambda} - \frac{\omega_r}{c} \right) \tag{3}$$

Dette er en postprint-versjon / This is a postprint version.
DOI til publisert versjon / DOI to published version: 10.1080/01431160210153039

where a_1, a_2 and ω_a are the Doppler centroid, azimuth Doppler rate and azimuth frequency, respectively. λ and c are the radar wavelength and the speed of light. Since the Doppler parameters are varying in cross–track direction phase correcting functions have been calculated in order to process large blocks, e.g. 2D FFT of size 2048 x 2048.

$$\Delta\phi(\omega_a, R, \hat{R}) = \left(\frac{a_1^2 \lambda k}{2 a_2} - \frac{\hat{a}_1^2 \lambda k}{2 \hat{a}_2}\right) + \left(\frac{a_1}{a_2} - \frac{\hat{a}_1}{\hat{a}_2}\right)\omega_a + \left(\frac{1}{2 a_2 \lambda k} - \frac{1}{2 \hat{a}_2 \lambda k}\right)\omega_a^2 \qquad (4)$$

where a_1 and a_2 are the Doppler parameters in the middle of a block at range R, and $\hat{a}_1$ and $\hat{a}_2$ the same parameters at a given range $\hat{R}$ within the block. In this way the ETF is extended to process a block and the algorithm has been called the EETF (Extended Exact Transfer Function). Obviously, the phase correction in equation (4) is zero in the middle of the block when $\hat{R} = R$. This algorithm does not assume linear range chirp as does the chirp scaling algorithm (Raney *et al.* 1994). The EETF copes with large Doppler centroid variations due to the multi–block processing approach. The chirp scaling algorithm assumes constant Doppler centroid. Furthermore, a minimum of FFTs and phase multiplications are needed, but still achieving the image quality requirements for operational SAR processing. The EETF2 SAR processor described above is a new approach and equation (4) has not been published elsewhere. The equations (1)–(4) are the basis for the core of the Kongsberg Spacetec SAR processor (Indregard *et al.* 1997). A 4th order ETF has also been calculated and new phase correcting functions up to 4th order have been calculated and implemented so that the processor is also phase preserving (Eldhuset 1998). Figure 2 shows an ERS SAR image over the region in frame 2 in figure 1 processed in slant range with the second–order EETF (EETF2) SAR processor. The estimation of Doppler parameters for the SAR processor is briefly described in Eldhuset (1996b). The EETF2 processor has also been used for generation of single look complex (SLC) data as input to a new method for wind field estimation (Engen *et al.* 1998, Høgda *et al.* 1998).

2.2 *Precise orbit determination and baseline estimation*

The baseline components have to be estimated by either preliminary (PRL) or precision (PRC) orbit data which were available for us from the ESA. We also used the FFI high precision GEOSAT software to compute the ERS orbits. The GEOSAT orbits used here were produced with the GEOSAT multipurpose space geodesy software (Andersen 1995). In this software, the most precise reference frames, dynamic models, and measurement models available are used and updated continually as better information comes along. A least–squares estimation method has been applied in the present analysis although a UD factorized Kalman filter implementation also is available in GEOSAT. A distinguishing feature of GEOSAT is that one and the same program can be used to analyze simultaneously, at the observation level, data from many different space platforms, e.g. Very Long Baseline Interferometry (VLBI), Global Positioning System (GPS), Satellite Laser Ranging (SLR), Precise Range and Range–rate Equipment (PRARE), Doppler Orbitography and Radio positioning Integrated by Satellite (DORIS), and Radar Altimetry (RA). The GEOSAT ERS–1 orbits used in the present analysis were produced from an analysis of SLR measurements. The ERS–2 orbits were determined from a simultaneous analysis of SLR and PRARE observations. Details of the processing strategy and the models can be found in Andersen *et al.* (1998).

The orbits are then used for estimation of the baseline components $B_y(t_a)$ (horizontal) and $B_z(t_a)$ (vertical) as a function of azimuth time t_a (see figure 7). It was found that $B_y(t_a)$ and

$B_z(t_a)$ could be very well approximated by linear polynomials over 100 km. We estimated the baseline components for an interferogram from 27/28 September 1995 using both PRL, PRC and GEOSAT orbits which are given in table 1. The GEOSAT interferogram is shown in figure 3. We can see from table 1 that the horizontal baseline components are quite similar for PRC and GEOSAT while there is constant difference of 8 cm in the vertical direction all over the scene. The baseline components estimated from the PRL orbits differ from those estimated from the precise orbits and the difference changes significantly over the scene which can be observed in the two interferograms in figure 4 (see last part of § 2.3). We estimated the baseline components for another interferogram which are given in table 2. The PRL, PRC, and GEOSAT all deviate a couple of decimeters, however, the differences in both the vertical and horizontal components are constant all over the scene. It should be noticed that the baselines are solely estimated from the precise orbital data and no control points in the SAR scene need to be used to remove reminiscent fringes as has been reported in the literature.

2.3 *Interferogram generation*

We used roughly the same steps for interferogram generation as in the literature (see. e.g. Lanari *et al.* 1996), however, we use here a more general model than in the literature. The phase compensation that is applied to the raw interferogram can be written (see figure 7)

$$\Delta\Phi(R, t_a) = 4\frac{\pi}{\lambda}\left(B_y(t_a)\sin\{\Theta(R, t_a)\} + B_z(t_a)\cos\{\Theta(R, t_a)\}\right) \qquad (5)$$

The usual way to compensate the raw interferogram is to use a locally flat earth model which allows analytical calculations of elevation (see e.g. Massonet 1995 , Lanari *et al.* 1996). Here we show that it is also possible to do analytical calculations (see § 3.2) if one uses an ellipsoid earth model. Equation (5) is applied to the raw interferogram to compensate the phase due to nonparallell orbits and the slant range phase. In equation (5) the baseline components $B_y(t_a)$ and $B_z(t_a)$ are functions of the azimuth time, t_a . The look angle $\Theta(R, t_a)$ is a function of both the slant range and the azimuth time, which is not taken into account in the literature. The look angle is a function of azimuth time since the satellite altitude varies in azimuth direction due to the satellite Kepler orbit around an ellipsoid earth. In this way one should get constant phase over flat regions coincident with the earth ellipsoid model. If there are rather steep hill sides along the sea one can also check how well the fringes follow the coast line. It is convenient to check how well the interferogram is compensated to an earth ellipsoid in this way because the fringes caused by the terrain need not be removed. In figure 3 is shown a multilook interferogram processed with the FFI INSAR processor and using the GEOSAT baseline components in table 1.

Prior to the estimation of the interferometric phase we averaged 4 complex samples in range direction and 16 samples in azimuth direction as was done in Kwock and Fahnestock (1996). In figure 4 is shown the region around Wijdefjorden zoomed from figure 3 (the multilooking is 4 samples in the azimuth direction). The upper interferogram was processed with baseline components estimated from GEOSAT orbits and the lower from PRL orbits. We can see that for the GEOSAT interferogram the fringe follows the coast line very well. In the literature many interferograms do not appear in this way, which means that the interferograms have not been flattened to an ellipsoid. For the PRL interferogram we can see that the fringes do not follow the coast line which can be explained by more inaccurate baseline components as was indicated in table 1. Although we have processed many PRL interferograms with high quality this example

Dette er en postprint-versjon / This is a postprint version.
DOI til publisert versjon / DOI to published version: 10.1080/01431160210153039

shows that the most precise orbits available should be used to secure high quality interferograms.

2.4 *Decorrelation due to INSAR processor*

For investigation of decorrelation properties due to natural changes, it is important to know that the INSAR processor is coherence preserving. This could be done by the unique ERS tandem data and the unique climate on Svalbard. The coherence images were generated in a standard way (see e.g. Gens and Genderen (1996)). We have investigated several tandem coherence images processed on Svalbard and found one site where the coherence is above 0.95 in two of the images. The baselines were also very small in these images as shown in table 3. One can expect that for 1–day ERS tandem interferograms that the temporal decorrelation could be quite small if the ground conditions are stable. If we assume that the the thermal decorrelation is small in regions with a high signal–to–noise–ratio (SNR), we can give an estimate of the decorrelation due to the INSAR processor. In table 3 are shown the figures for the estimated coherence, γ_{tot} , which was estimated in a window of size 12 x 17 in a 4 x 16 multilook coherence image. γ_B is the baseline decorrelation factor. The standard deviation, σ_γ is also provided. In Lee (1994) it is shown that the coherence is independent of the number of looks, hence, it is advantageous to average as many pixels as possible (if the coherence is constant over the area) to reduce the variance of the coherence estimate. We expected that the temporal decorrelation was very small for these scenes since the temperature was between –10 and –5 degrees Celcius and no precipitation. From table 3 we have

$$\gamma_{SNR}\,\gamma_{temporal}\,\gamma_{proc} = \frac{\gamma_{tot}}{\gamma_B} = 0.977 \tag{6}$$

If we assume that the temporal and thermal decorrelation are both negligible, the decorrelation due to the INSAR processor is according to table 3 less than 0.977. In Bamler (1993) the different sources of decorrelation in an INSAR processor is described. These include relative geometric misregistration in azimuth (wrong FM rate) of range (wrong chirp rate or secondary range compression) of the two SLC scenes used for interferogram generation, defocusing in range and azimuth (wrong FM rate), uncompensated linear range migration and uncompensated quadratic range migration. These effects are analyzed in the above mentioned paper. We use the results in Bamler (1993) and assume that the two SLC scenes are misregistrated with 0.1 pixels in range. Then the decorrelation would be about 0.977 for large SNR. Since the temporal and thermal decorrelation may be slightly less than 1, the misregistration of the SLC scenes is probably below 0.05 pixels in both azimuth and range. This was actually the subsampling used during the registration of the SLC scenes. Hence, we may conclude that the other decorrelating factors in the INSAR processor are very small. In addition the thermal and temporal decorrelation must be negligible.

3. DEM generation using an INSAR simulator

3.1 *INSAR simulation*

In this work we use the NPI reference DEM to unwrap the real interferograms since unwrapping may be a difficult task without using existing DEMs. The first part of the INSAR DEM generation program is identical to that used in the FFI automatic ship detector (Eldhuset

1996a). This module performs a simple simulation of a SAR image taking into account the fold–over effect. This synthetic image is then correlated with the real SAR image. Only a small subimage in the scene is needed to find an offset in range and azimuth. The offset in azimuth is mainly due to the uncertainties in the orbital state vectors (may be several hundred meters for predicted state vectors). The simulation of an unwrapped interferogram is then performed by using the orbital state vectors of one of the orbits (at least PRL data) and a pixel location algorithm described in Curlander (1982). The estimated baseline components are used to re–calculate the second orbit. Then the two–way path difference is calculated according to

$$\Phi = \frac{4\pi}{\lambda}\left(R_1 - R_2\right) \tag{7}$$

where R_1 and R_2 are defined in figure 5 and are the slant ranges between a point P on the DEM and the satellite positions S_1 and S_2 (e.g. of ERS–1 and ERS–2). The phase compensation given in equation (5) is then subtracted from the the phase computed by equation (7). The input DEM that is used here had 50 m pixel spacing and is rotated and interpolated with splines. A resampling of factor 4 gives excellent quality of the wrapped simulated interferogram. The real interferogram is then unwrapped using the unwrapped simulated interferogram. A simulated interferogram in the same region as in figure 3 is shown in figure 6. By counting the number of fringes from the fjord to the top of the mountain in figure 3 and figure 6 it can be verified that the number of fringes is the same, hence, there is a geometrical consistency (see also Franceschetti 1998) between the real and the simulated interferogram.

3.2 *DEM generation*

There are a number of articles giving equations for height as a function of the unwrapped phase in the interferogram e.g. (Gens *et al.* 1996), (Massonet *et al.* 1993), or (Massonet *et al.* 1995). The formulas in the mentioned references are either for a flat earth, or a plane tangential to the earth where the height is to be estimated. In (Massonet *et al.* 1993) the altitude of ambiguity is defined, which is the height corresponding to a phase change of 2π. Here we calculate an expression based on an ellipsoid earth model which has not been published previously. First we have to calculate the phase difference (continuous phase) for two points P_1 and P_2 with height h (see figure 7)

$$\Delta\Phi = \frac{4\pi}{\lambda}\left(\left(B_y \sin(\Theta) - B_z \cos(\Theta)\right) - \left(B_y \sin(\Theta + \Delta\Theta) - B_z \sin(\Theta + \Delta\Theta)\right)\right) \tag{8}$$

where $\Delta\Theta$ is the look angle difference for the two points. The phase difference in equation (8) is defined as

$$\Delta\Phi = \Phi_1 - \Phi_2 \tag{9}$$

(see figure 7). If we expand equation (8) and assume that $\Delta\Theta$ is small, $\Delta\Theta$ can be found by

$$\Delta\Theta = \operatorname{asin}\left(\frac{\lambda}{4\pi}\,\frac{\Delta\Phi}{B_y \cos(\Theta) + B_z \sin(\Theta)}\right) \tag{10}$$

Dette er en postprint-versjon / This is a postprint version.
DOI til publisert versjon / DOI to published version: 10.1080/01431160210153039

In figure 8 it is shown how the height can be calculated from the look angle difference when the earth is modelled as an ellipsoid. S_1 is one of the satellites and E is the center of the earth. The two points P_1 and P_2 are in the same range from the satellite. The vectors EP_1 and EP_2 are almost parallell since the look angle difference is very small. We can calculate EP_1 which is the distance from the earth center to the earth's surface using the cosine rule

$$R_E = \sqrt{R_S^2 + R^2 - 2 R_S R \cos(\Theta)} \tag{11}$$

In the same way the distance from the earth center E to the point P_2 at height h above the earth reference ellipsoid is

$$R_E + h = \sqrt{R_S^2 + R^2 - 2 R_S R \cos(\Theta + \Delta\Theta)} \tag{12}$$

The radius of the satellite, ES_1 is calculated during the interferogram simulation and the distance R is given by the distance to the first sample plus the number of samples to point P_1. The look angle difference is found by equation (10). Taking the difference of equation (11) and equation (12) yields the height h

$$h = \sqrt{R_S^2 + R^2 - 2 R_S R \cos(\Theta + \Delta\Theta)} - \sqrt{R_S^2 + R^2 - 2 R_S R \cos(\Theta)} \tag{13}$$

The ambiguity of altitude can be calculated by equation (13) by inserting equation (10) with $\Delta\Phi = 2\pi$. B_y and B_z are as mentioned functions of azimuth time, hence, the altitude of ambiguity is a function of both range and azimuth. In the case of tandem geometry the B_y component of the baseline may change several meters over one scene (see tables 1 and 2).

3.3 *Assessment of the INSAR DEM*

Several interferograms were processed over the same site in order to check the quality of the INSAR DEM. The test region covered an area of 70 km in range and 82 km in azimuth around Åsgårdfonna and Wijdefjorden, see figures 1 and 2. The baseline components used for generation of the interferogram in figure 3 were estimated from orbits computed by GEOSAT. The region shown in figure 3 was divided into 5 x 5 blocks and then the mean difference height and the (root–mean–square) RMS of the INSAR DEM and the NPI DEM were estimated in each block. The figures in table 4 without brackets are the the mean difference heights and the figures with brackets correspond to the RMS in each block . Table 5 shows the mean height in each block of the INSAR DEM. We see that the RMS is typically between 10 and 20 meters which can be expected in hilly terrain. However, the mean differences are pretty good and indicate that the INSAR DEM is of high quality.

The same assessment as above was done for an INSAR DEM generated from another interferogram with somewhat larger baselines also estimated from GEOSAT orbits. The mean difference heights and the RMS values for each block are shown in table 6. Tables 4 and 6 indicate that there is no linear drift in the height differences in azimuth nor in range. It should be noted that only one reference height is used within this region. That means that when equation (13) together with equation (10) the phase in every point of the interferogram is measured relative to

Dette er en postprint-versjon / This is a postprint version.
DOI til publisert versjon / DOI to published version: 10.1080/01431160210153039

one and the same reference phase (which is an average over some pixels). We also observe that the RMS values in tables 4 are somewhat larger than in table 6 which is an effect of smaller baseline for the case in table 4. We generated several INSAR DEMs in the same region with different baselines and found that there is a clear trend of increasing RMS when the baseline gets smaller as shown in table 7.

We have used both PRC, PRL and GEOSAT orbit data. For many of the interferograms we have not found any significant improvements in the INSAR DEM quality or fringe quality by using PRC instead of PRL which has also been concluded in Reigber *et al.* 1997. We could not observe any further improvement using GEOSAT orbits, although GEOSAT orbits may be somewhat better than the PRC orbits. In the region shown in figure 3 we used both GEOSAT and PRL orbits for baseline estimation. We found that there was only minor differences (less than 1 m) between the INSAR DEMs generated from GEOSAT and PRL orbits. This is due to the method used: A simulated unwrapped interferogram was used to unwrap the real interferogram, hence, there will be no drift in the height estimates in the region. If no reference DEM were available one might risk larger drift in the heights using PRL data than using PRC or GEOSAT orbits.

Figure 9 shows a differential interferogram where the simulated interferogram (using the NPI DEM) has been subtracted from the real interferogram in the lower part of figure 3. The upper image has been processed using baseline components estimated from GEOSAT orbits and the lower has been processed with PRL orbits. We clearly see the rest fringes in the lower image while in the upper image the phase drift is much smaller. A perfect differential interferogram should be of constant phase apart from the fringes generated by moving glaciers or atmospheric effects.

4. Ice velocity estimation on the Kronebreen glacier

The first paper on estimation of glacier motion using interferometry appeared in Goldstein *et al.* (1993). They used ERS–1 for estimation of the speed of the Ruthford Ice Stream in Antarctica in a rather flat region. Others estimated ice sheet motion on Greenland (e.g. Kwock *et al.* 1996), but they did not have DEM available and had to use differential interferometry with two 3 day interferograms to isolate the effect of the topography. In Mattar *et al.* (1998) and in Cumming *et al.* (1997) ERS tandem data were used for estimation of glacier flow where they used a DEM obtained from an aircraft interferometer to simulate the effect of topography. They found very good agreement with ground measurements. In addition, the fringes in the interferogram were easily countable. Our selected glacier, called Kronebreen, is more demanding because of higher speed and crevasses. The NPI DEM was based on traditional topographic methods and partly by photogrammetric methods.

Kronebreen is one of the most active calving glaciers on Svalbard. It is a tidewater glacier and is located in Kongsfjorden, see frame 1 in figure 1. Figure 10 shows a SAR image from this region. Kronebreen has an area of 690 km^2 and Kongsvegen has an area of 189 km^2. Figure 11 shows a differential tandem interferogram over Kronebreen and Kongsvegen. This differential interferogram has almost uniform phase over Kongsvegen which indicate very small motion while Kronebreen has numerous complicated fringes.

4.1. *Technique for speed estimation*

We used similar methods as in Goldstein *et al.* (1993) and Kwock *et al.* (1996). The formula given below was used for estimation of the speed of the glacier, V_{glac}

$$V_{glac} = \frac{\left\{n_{fringes} \cdot \frac{\lambda}{2}\right\}}{\{\cos\epsilon \cos\psi \sin\theta + \cos\theta \sin\epsilon\}} \quad (14)$$

where ϵ is the slope of the glacier surface relative to the earth's ellipsoid, θ is the look angle for a given point on the glacier, ψ is the angle between the horizontal component of the glacier velocity vector and the range direction in the SAR image and $n_{fringes}$ is the numbers of fringes counted in the interferogram if the effect of the terrain relief has been subtracted. It is assumed that ϵ, ψ and θ in equation (14) are constant for the number of fringes, $n_{fringes}$, over a given region.

4.2. *Comparison of ice estimates using INSAR and photogrammetry*

Figure 12 shows a 4–look differential interferogram around the Kronebreen glacier. The fringes along a longitudinal profile (along the line LL in figure 10) on Kronebreen were counted in figure 12 and translated to ice velocities as shown in figure 13. The fringes are clear in the upper part of the glacier but get more noisy downstream and towards the edges.

Our study suggests that the ice velocity in the upper part of Kronebreen is on the order of 0.5 m/day. Interesting is that data from another interferometry project concerning Holtedahlfonna and Isachsenfonna, upstream Kronebreen, give the same ice velocity for the overlapping area on Kronebreen (Lefauconnier and others, unpublished data). In that case a 6 days interferogram was used.

In the area 5–10 km from the glacier front the velocity profile reveals a peak with velocities above 2 m/day. The velocity decrease to around 1 m/day below this area. On a tide–water glacier like Kronebreen the velocity should increase towards the front, and the reason for what we see in this profile is most likely that the fringes cannot be resolved in the lower part of the glacier and the velocity is underestimated. Unfortunately, there are few other velocity data to compare to and the available data are all concentrated on the lower 1–2 km of Kronebreen, where fringes are impossible to interpret from the interferogram.

In a 4 km transverse profile (the line TT in figure 10), about 5 km from the ice front, the ice velocities obtained from figure 12 can be compared with previous velocity data calculated from terrestrial photogrammetry (Melvold, 1992). In figure 14 we can see that the distribution of ice velocity agrees well between these studies but the velocities obtained from the interferogram is up to 50 % lower than the data from photogrammmetry. The interferogram is from April 5–6 1996 and the photogrammetry data a daily mean from the period May 5–27 1990. Because both these ice velocity datasets are originating during the same time of the year it is not likely that the seasonal variations is the reason to the velocity differences. According to a study of surface velocities over one year in the period 1964–1965 the ice velocity was found to be almost constant between October to mid–June and then increase by a factor of two at the end of June (Pillewizer *et al*. 1967, Voigt 1969). In September the velocity decreased to half the annual value. The difference in ice velocity between the months May and August is on the order of 65% according to the photogrammetry study by Melvold (1992). The most likely explanation for the velocity difference that we see is that the noisy fringe pattern along the edges of Kronebreen,

Dette er en postprint-versjon / This is a postprint version.
DOI til publisert versjon / DOI to published version: 10.1080/01431160210153039

particularly along the southern side of the glacier, cannot be resolved. Further up–stream the glacier the fringe pattern is much better developed also along the edges, but unfortunately, there are no other velocity measurements for comparison. However, the magnitude of the velocity is what can be expected in this part of the glacier.

We processed differential interferograms over the region shown in figure 1 in frame 1 in the tandem period 1995/1996 in July, August, September, January, February, March, April and May. It is obvious that the fringe pattern in the upper part of Kronebreen is almost the same for all months. In the lower part, the central area seem to be very stable, however, along the sides it is difficult to count fringes due to the noisy fringe pattern. During the tandem period the ice velocity seems to be stable and not increased in the summer time as observed by Melvold (1992). More glaciers in both frame 1 and 2 in figure 1 were analyzed using the differential interferograms processed here, see Wangensteen (1998) and Wangensteen *et al.* (1998).

The conclusion of the analysis of fringes suggests that even with the short time period of one day the interferograms are noisy at the fast–moving front of Kronebreen and in the contact zone with Kongsvegen. The most likely explanation for this is probably the high shear in these parts of the glacier, suggested by the complicated crevasse patterns. It is also possible that the very large velocity difference between Kronebreen and Kongsvegen contribute to the noisy fringe pattern in the contact zone between these glaciers. In the contact area between these glaciers Kronebreen has ice velocities of more than 2 m/day while velocities on Kongsvegen are in the order of 1–2 cm/day (Melvold 1992, Lefauconnier *et al.* 1994, Rolstad 1995). It seems that on a fast–moving glacier like Kronebreen, where parts of the glacier are heavily crevassed, a combination of field measurements, photogrammetric methods and interferometry are necessary to obtain a complete picture of ice velocities (Isaksson *et al.* 1996).

The FFI INSAR processor combined with precise orbits from GEOSAT was also used to generate 3 day interferograms for estimation of the speed of the large ice stream called Jutulstraumen in Dronning Maud Land, Antarctica. The fringes were much easier to count than on Kronebreen and the maximum speed of Jutulstraumen is about 2 m/day (Rolstad *et al.* 1997, Rolstad 2000).

5. Coherence analysis

There are examples that interferometric SAR coherence measures can be used for vegetation classification (Wegmuller and Werner 1997, Askne and Hagberg 1993) and glaciological studies (Rott and Siegel 1996). The coherence is given by the complex correlation between two co–registered single look complex interferometric SAR image pairs.

For the SAR images studied here, the coherence was estimated using a window size of 3x15 pixels in slant range and azimuth respectively (i.e. 45 averaging pixels). This gives a pixel size of approximately 60 m x 60 m for the resulting coherence image. Several test areas of 1 km^2 in size were selected from glaciers and valleys at Svalbard. The mean coherence was then calculated from these areas using eight tandem SAR image pairs acquired in 1995 and 1996. Results from the Kronebreen and Kongsvegen glaciers as well as a rock/bare soil area near to Ny–Ålesund are plotted in figure 15. Results from the other test areas at Svalbard can be found in (Weydahl 1998 and Weydahl 2001).

Dette er en postprint-versjon / This is a postprint version.
DOI til publisert versjon / DOI to published version: 10.1080/01431160210153039

Changes in backscatter properties from the ground surface (roughness, moisture, thawing conditions) may lead to changes in the measured coherence. Air temperatures and precipitation are therefore collected from the Ny–Ålesund meteorological station at Svalbard to aid in the interpretation of the coherence in figure 15. Temperatures in July 1995 indicate that the glacier surfaces were in a melting/thawing condition. This gives low SAR coherence from these areas. The high coherence (0.87) observed from the Ny–Ålesund area is due to a stable backscatter situation (no precipitation) from the sparse vegetation and rock surface. In August, the higher elevation parts of the glaciers do not undergo the same scattering changes as in July, while the lower elevation parts still experience thawing.

In January, the Ny–Ålesund meteorological station registered average temperatures of –0.4°C and –4.1°C as well as 18.6 mm and 6.9 mm precipitation at the SAR tandem data takes the 10 and 11 January 1996. The coherence from the Ny–Ålesund test area (as well as from some glacier surfaces) was dramatically reduced in the January image (0.26) as compared to August (0.90). This high temporal decorrelation can be explained by rainfall or sleet in the lower elevation regions.

A complex weather situation with temperatures down towards –32°C in February, and possible rainfall before the acquisitions in March, made it difficult to link the coherence values directly to temperature and precipitation recordings for these acquisitions. The April data set gave extremely high coherence values (> 0.92) from the test areas shown in figure 15, which may be due to stable weather conditions with air temperatures around –8°C.

As found in § 4.2 Kronebreen has a mean speed of 2.0 m per day throughout the year (see also Lefauconnier *et al.* 1994). This velocity leads to decorrelation in the tandem SAR data as can be seen from the mean coherence profiles in figure 15 (”Kronebreen – lower part”) and the April coherence image shown in figure 16. Similarly, the shear zones that experience surface deformation and rotation of ice–blocks at the sides of Kronebreen, is detected by its low coherence.

6. Conclusions

The INSAR processing algorithms at FFI have been described and the ERS tandem data were used to assess the performance. It was demonstrated that the INSAR processor achieved coherence close to 1 for very small baselines. The fringes in the ellipsoid flattened interferograms follow the coastline pretty well using both GEOSAT, PRC and PRL orbits, however, we demonstrated that PRL orbits may provide considerably reduced interferogram flattening. The RMS of the INSAR DEM varied between 7 and 20 m. Although one–day interferograms were used, a combination of field measurements, photogrammetric methods and interferometry are necessary to obtain a complete pattern of ice velocities on a fast–moving glacier like Kronebreen (maximum 2 m/day), where parts of the glacier are heavily crevassed. A time series of differential interferograms showed that the fringe pattern of Kronebreen generated by the motion was quite stable in the period from July 1995 to May 1996. It has also been demonstrated that considerable decorrelation may occur in tandem interferograms if the ground conditions on snow and glaciers are changing.

Acknowledgment. This paper presents results from the ESA Announcement of Opportunity Project, AOT.N301, and was mainly supported by FFI and partially by NPI and the Norwegian

Space Centre. The tandem raw data were provided by ESA and the algorithms for interferogram generation were industrialized by Kongsberg Spacetec (Indregard *et al.* 1997) under a WEAG (Western European Armaments Group) EUCLID (EUropean Cooperation for the Long term In Defence) project (Tyridal 1997). Special thanks go to Director of Research H. K. Johansen and Chief Scientist T. Wahl (Chairman of RTP 9.4 Management Group) at FFI for encouraging this work. The EETF algorithm has been industrialized by Kongsberg Spacetec (http://www.spacetec.no) for RADARSAT and ERS processing and delivered to the satellite stations in Tromsø, Singapore, Istanbul, Hiroshima, Argentina and Egypt. Finally, thanks to Jostein Amlien at NPI for providing the reference DEM.

References

ANDERSEN, P.H., 1995, High–precision station positioning and satellite orbit determination, NDRE/PUBLICATION–95/01094, Norwegian Defence Research Establishment.

ANDERSEN, P.H., AKSNES K., SKONNORD H., 1998, Precise ERS–2 orbit determination using SLR, PRARE, and RA observations, *Journal of Geodesy,* **72**, pp. 421–429.

ASKNE, J., HAGBERG, J. O., 1993, Potential of interferometric SAR for classification of land surfaces, *Proceedings of the International Geoscience and Remote Sensing Symposium (IGARSS'93), Tokyo, 18–21 August 1993,* (Piscataway:I.E.E.E.), pp. 985–987.

BAMLER, R., JUST, D., 1993, Phase statistics and decorrelation in SAR interferograms, *Proceedings of the international Geoscience and Remote Sensing Symposium (IGARSS'93), Tokyo, 18–21 August 1993,* (Piscataway:I.E.E.E), pp. 980–984.

CHANG, C.Y., JIN, M.Y., CURLANDER, J.C. , 1992, SAR Processing Based on the Exact Two–Dimensional Transfer Function, *Proceedings of the International Geoscience and Remote Sensing Symposium (IGARSS'92), Houston, Texas, 26–29 May 1992,* (Piscataway:I.E.E.E.), pp. 355–359.

CUMMING, I., VALERO, J–L., VACHON, P., MATTAR, K., GEUDTNER, D., GREY, D., 1997, Glacier Flow Measurements with ERS Tandem Mission data, *Proceedings of the 'Fringe 96' Workshop on ERS SAR Interferometry, Zurich, 30 September–2 October,* (Noordwijk:ESA), pp. 353–362.

CURLANDER, J.C., 1982, Location of spaceborne SAR imagery , *I.E.E.E. Transactions on Geoscience and Remote Sensing,* **20** , pp. 359–364.

ELDHUSET, K., 1995, Fast phase preserving processing of spaceborne SAR data, FFI/RAPPORT–95/00644, Norwegian Defence Research Establishment.

ELDHUSET, K., 1996a, An automatic Ship and Ship Wake Detection System for Spaceborne SAR Images in Coastal Regions , *I.E.E.E. Transactions on Geoscience and Remote Sensing,* **34**, pp. 1010–1019.

ELDHUSET, K., 1996b, Accurate attitude estimation using ERS–1 SAR raw data , *International Journal of Remote Sensing,* **17**, pp. 2827–2844.

ELDHUSET, K., 1998, A new fourth order processing algorithm for spaceborne SAR. *I.E.E.E. Transactions on Aerospace and Electronic Systems,* **34,** pp. 824–835.

ENGEN, G., HØGDA, K.A., JOHNSEN, H., 1998, A new method for wind field retrieval from SAR data, *Proceedings of the CEOS SAR Workshop, ESTEC, Noordwiijk, 3–6 February 1998,* (Noordwiijk:ESA), pp. 47–51.

FRANCESCHETTI, G., IODICE, A. , MIGLIACCIO, M. , RICCIO, D., 1998, Simulation of SAR Interferometric Raw Signal Pairs Corresponding to Real Scenes, *Proceedings of the Inter-*

national Geoscience and Remote Sensing Symposium (IGARSS'98), Seattle, 6–10 July 1998, (Piscataway:I.E.E.E.), pp. 2653–2655.

GENS, R., GENDEREN VAN, J.L., 1996, Review article, SAR interferometry–issues,techniques, applications , *International Journal of Remote Sensing,* **17**, pp. 1803–1835.

GOLDSTEIN, R.M., ZEBKER, H.A., WERNER, C.L., 1988, Satellite radar interferometry: Two–dimensional phase unwrapping , *Radio Science,* **23**, pp. 713–720.

GOLDSTEIN, R.M., ENGELHARDT, H., KAMB, B., FROLICH, R.M. ,1993, Satellite Radar Interferometry for Monitoring Ice Sheet Motion: Application to an Antarctic Ice Stream , *Science,* **23**, pp. 1525–1530.

HØGDA, K.A., ENGEN, G. , JOHNSEN, H. , 1998, Wind Field Estimation from SAR Ocean Images, *Proceedings of the International Geoscience and Remote Sensing Symposium (IGARSS'98), Seattle, 6–10 July 1998,* (Piscataway:I.E.E.E.), pp. 945–948.

INDREGARD, M., ELDHUSET, K., JOHNSEN, H., HØGDA, K.A., 1997, Phase properties of SAR algorithm, WEAG EUCLID RTP 9432.13, Kongsberg Spacetec final report.

ISAKSSON, E., AMLIEN, J., LEFAUCONNIER, B., ROLSTAD, C. , ELDHUSET, K., ANDERSEN, P.H., HAUGE, S., MELVOLD, K., 1996, SAR interferometry used to derive ice velocities on Kronebreen, Svalbard, *American Geophysical Union Fall Meeting 15–19 December 1996, In Eos.,* **77***(46)* .

KWOK R., FAHNESTOCK, M.A., 1996, Ice Sheet Motion and Topography from Radar Interferometry , *I.E.E.E. Transactions on Geoscience and Remote Sensing,* ***34***, pp. 189–200.

LANARI, L., FORNARO, G., RICCIO, D., MIGLIACCIO, M., PAPATHANASSIOU, K.P., MOREIRA, J.R., SCHWAEBISCH, M., DUTRA, L., PUGLISI, G., FRANCESCHETTI, G., COLTELLI, M., 1996, Generation of Digital Elevation Models by Using SIR–C/X–SAR Multifrequency Two–Pass Interferometry: The Etna Case Study, *I.E.E.E. Transactions on Geoscience and Remote Sensing,* ***34***, pp. 1097–1114.

LEE, J–S., HOPPEL, K.W., MANGO, S.A., MILLER, A.R., 1994, *I.E.E.E. Transactions on Geoscience and Remote Sensing,* **32** , pp. 1017–1028.

LEFAUCONNIER, B., HAGEN, J.O., RUDANT, J.P., 1994, Flow speed and calving rate of Kronebreen glacier, Svalbard, using SPOT images. *Polar Research,* **13**, pp. 59–65.

MASSONET, D., RABAUTE, T., 1993, Radar Interferometry: Limits and Potential , *I.E.E.E. Transactions on Geoscience and Remote Sensing,* ***31***, pp. 455–464.

MASSONET, D., VADON, H., 1995, ERS–1 Internal Clock drift Measured by Interferometry , *I.E.E.E. Transactions on Geoscience and Remote Sensing,* ***32***, pp. 401–408.

MATTAR, K.E., VACHON, P.W., GEUDTNER, D., GREY, A.L., CUMMING, I.G., BRUGMAN, M., 1998, Validation of Alpine Glacier Velocity Measurements Using ERS Tandem–Mission SAR Data, *I.E.E.E. Transactions on Geoscience and Remote Sensing,* ***36***, pp. 974–983.

MELVOLD, K., 1992, Study of glacier motion on Kongsvegen and Kronebreen, Svalbard. Technical Report, Department of Geography, University of Oslo, Norway.

PILLEWIZER, L. *et al.*, 1967. Die wissenschaftlichen Ergebnisse der deutschen Spitsbergenexpedition 1964–65. Bewegungsmessungen an Kongsvegen und Kronebree. *Geod. Geoph. Veröff. R III, H12*, Berlin 1967.

RANEY, R.K., RUNGE, H., BAMLER, R., CUMMING, I.G., WONG, F.H., 1994, Precision SAR processing using chirp scaling, *I.E.E.E. Transactions on Geoscience and Remote Sensing*, **32**, pp. 786–799.

REIGBER, C., XIA, Y. , KAUFMANN, H., MASSMANN, F.H., TIMMEN, L., BODECHTEL, J., FREI, M., 1997, Impact of Precise Orbits on SAR Interferometry, *Proceedings of the 'Fringe96' Workshop on ERS SAR Interferometry, Zurich, 30 September–2 October 1996*, (Noordwijk:ESA), pp. 223–232.

ROLSTAD, C., AMLIEN, J., ANDERSEN, P.H., ELDHUSET, K., HAGEN, J.O., HAUGE, S., ISAKSSON, E., WINTHER, J.G., 1997, Determination of glacier velocity on Jutulstraumen, Dronning Maud Land, using Landsat TM and ERS–1 SAR, *Symposium on Antarctica and Global Change:Interactions and Impacts, Tasmania, 13–17 July 1997.*

ROLSTAD, C., 1995, Satellite –and aircraft images for determination of glacier dynamics (In Norwegian), Master thesis, Department of Geography, University of Oslo, Norway.

ROLSTAD, C., 2000, The large–scale dynamics of Jutulstraumen drainage basin, East Antarctica , PhD Thesis, Department of Geography, University of Oslo, Norway.

ROTT, H., SIEGEL, A., 1996, Glaciological studies in the Alps and in Antarctica using interferometric SAR, *Proceedings of the 'Fringe96' Workshop on ERS SAR Interferometry, Zurich, 30 September–2 October 1996*, (Noordwijk:ESA), Vol 2, pp. 149–159.

TYRIDAL, P., 1997, Real Time Processing and Data Handling Technology, Programme Final Report, WEAG EUCLID RTP 9.4, Kongsberg Informasjonskontroll.

VOIGT, U., 1969, Ergebnisse der Bewegungsmessungen an Kongsvegen und Kronebree. Wissenschaftlichen Ergebnisse der Deutschen Spitsbergenexpedition.

WANGENSTEEN, B., 1998, Estimation of glacier movement on Svalbard using satellite SAR interferometry (In Norwegian), Master Thesis, Department of Geography, University of Oslo, 1998.

WANGENSTEEN, B., WEYDAHL, D.J., HAGEN, J.O., 1998, Mapping Glacier Velocities at Spitsbergen Using ERS Tandem SAR Data, submitted to *International Geoscience and Remote Sensing Symposium (IGARSS'98), Hamburg, 28 June–02 July 1999.*

WEGMULLER, U., WERNER, C., 1997, Retrieval of vegetation parameters with SAR interferometry, *I.E.E.E. Transactions on Geoscience and Remote Sensing*, **35**, pp. 18–24.

WEYDAHL, D.J., 1998, Analysis of satellite SAR images for change detection over land areas, PhD Thesis, Department of Geography at University of Oslo, FFI/PUBLICATION–98/04969, Norwegian Defence Research Establishment.

WEYDAHL, D.J., 2001, Analysis of ERS Tandem SAR Coherence From Glaciers, Valleys, and Fjord Ice on Svalbard, *I.E.E.E. Transactions on Geoscience and Remote Sensing*, **39**, pp. 2029–2039.

Figure 1 Map over the two test regions on Svalbard.

Figure 2 ERS–1 slant range SAR image in frame 2 of figure 1 in the region around Åsgårdfonna, 27 September 1995, orbit 21969, frame 1971. The image covers 70 km in range and 82 km in azimuth.

Figure 3 64–look tandem interferogram from Svalbard in the region around Åsgårdfonna, scenes 27/28 September 1995 (same region as in figure 2).

Figure 4 4–look interferogram in the region around Wijdefjorden in the lower right part of figure 3. The upper image has been processed with baselines estimated from GEOSAT orbits and lower image from PRL orbits.

Figure 5 Sketch for interferogram simulation. The DEM is based upon a reference earth ellipsoid (e.g. ED 1950).

Figure 6 Simulated interferogram in the same region as in figure 3.

Figure 7 Interferometric geometry used for calculation of look angle difference of two points, P_1 and P_2 with height difference h. The earth's curvature and the base line components are exaggerated.

Figure 8 Geometry for calculation of height h as a function of look angle difference, $\Delta\theta$. The point P_1 is on the reference ellipsoid of the earth and P_2 is at a height h above the ellipsoid. Note that the angle $\Delta\theta$ is very small.

Figure 9 64–look differential interferogram in the region around Wijdefjorden in figure 3. Upper image has been processed with baselines estimated from GEOSAT orbits and lower image from PRL orbits.

Figure 10 ERS–1 SAR image over Isachsenfonna, Kronebreen and Kongsvegen in frame 1 in figure 1, 5 April 1996, orbit 24703, frame 1989.

Figure 11 36–look differential tandem interferogram (5/6 April 1996) in the same region as in figure 10.

Figure 12 4–look differential tandem interferogram (5/6 April 1996) around Kronebreen in figure 11.

DOI til publisert versjon / DOI to published version: 10.1080/01431160210153039

Figure 13 Ice velocity along a longitudinal profile on Kronebreen. Data from velocity measurements performed with other methods only exists from the lowermost 5km of the glacier and they reveal higher velocities than obtained with interferometry. The data included in the figure are as follows; the photogrammetry study, mean value from one year of measurements 1964–1965 (Pillewizer et al., 1967: Voigt, 1969); SPOT 1, mean from the period August 8 to September 7 1986 (Lefauconnier et *al.*, 1994); SPOT 2 August 8 to September 7 1986 (Rolstad, 1995) and the interferometry, April 5–6 1996 (this study).

Figure 14 Ice velocity along a transverse profile about 5 km from the ice front. The interferometry data is from April 5–6 1996 and the photogrammetry data is a mean from the period May 5–27 1990 (Melvold, 1992). Garwoodtoppen is on the left hand side and Colletthøgda on the right which means that the ice flow is into the figure.

Figure 15 The mean ERS SAR coherence from various test areas plotted for eight interferometric tandem pairs. The coherence data are not corrected for the baseline effect, but the dates marked with * indicate the cases with the longer baselines (131–172 m). Decorrelation due to these longer baselines will typically lead to coherence values that are lower than 0.85.

Figure 16 Two tandem SAR coherence images showing Kronebreen, Kongsvegen and Ny–Ålesund on Svalbard. The August image decorrelates due to melting surface conditions on the glaciers. The parts of the moving Kronebreen glacier that experience deformation shear, are clearly detected by its low coherence in the April image.

Table 1 Baseline components By1 and Bz1 at the start of scene from Wijdefjorden 27/28 September 1995 and baseline components By2 and Bz2 at the end of the scene.

	$B_{y1}(m)$	$B_{z1}(m)$	$B_{y2}(m)$	$B_{z2}(m)$	$\Delta t_a(s)$
PRL	132.00	–9.00	140.26	–8.82	17.0
PRC	131.93	–8.96	140.06	–9.09	17.0
GEOSAT	131.93	–9.04	140.04	–9.17	17.0

Table 2 Baseline components By1 and Bz1 at start of scene from Wijdefjorden 20/21 March 1996 and baseline components By2 and Bz2 at the end of the scene.

	$B_{y1}(m)$	$B_{z1}(m)$	$B_{y2}(m)$	$B_{z2}(m)$	$\Delta t_a(s)$
PRL	193.43	–11.67	189.05	–12.28	16.0
PRC	193.72	–11.69	189.34	–12.30	16.0
GEOSAT	193.50	–11.66	189.12	–12.27	16.0

Table 3 Assessment of INSAR processor in terms of coherence

Image	γ_{tot}	σ_γ	γ_B	$\frac{\gamma_{tot}}{\gamma_B}$	$B_y\,(m)$	$B_z\,(m)$
05/06April	0.965	0.008	0.988	0.977	11.80	1.17
10/11 May	0.898	0.028	0.917	0.979	–78.85	–6.92

Dette er en postprint-versjon / This is a postprint version.
DOI til publisert versjon / DOI to published version: 10.1080/01431160210153039

Table 4 The mean difference height and the RMS (in brackets) between the NPI DEM and the INSAR DEM, Svalbard 27/28 September 1995, in sub regions of the area in figure 2. The size of each block is 14 km in range x 16.4 km in azimuth. The GEOSAT baseline components in table 1 were used for interferogram generation.

–2.7 (9.0)	*9.0 (15.0)*	*–7.6 (14.8)*	*–2.2 (15.0)*	*8.8 (20.8)*
–5.9 (8.5)	*0.6 (9.0)*	*–0.2 (15.9)*	*3.3 (15.2)*	*10.4 (15.6)*
–7.8 (12.8)	*4.1 (14.8)*	*–4.0 (11.4)*	*–2.9 (14.3)*	*–4.8 (14.2)*
–8.4 (17.6)	*5.1 (14.2)*	*–1.1 (12.7)*	*–7.4 (14.0)*	*–5.5 (10.9)*
–7.5 (14.8)	*4.9 (19.9)*	*1.9 (12.9)*	*–5.8 (9.0)*	*–9.5 (14.1)*

Table 5 Mean of heights in the same blocks as in the region in table 4.

0.9 m	*200.5 m*	*258.4 m*	*548.3 m*	*944.5 m*
6.4 m	*61.1 m*	*344.8 m*	*891.4 m*	*796.4 m*
93.0 m	*579.7 m*	*778.9 m*	*839.7 m*	*227.5 m*
138.9 m	*492.7 m*	*607.7 m*	*237.2 m*	*245.5m*
46.5 m	*248.8 m*	*138.4 m*	*87.4 m*	*599.2 m*

Table 6 The mean difference height between the NPI DEM and the INSAR DEM, Svalbard 20/21 March 1996. The size of each block is 14 km in range x 16.4 km in azimuth. The GEOSAT baseline components in table 2 were used for interferogram generation.

–2.6 (4.4)	*–1.4 (7.1)*	*–1.0 (12.2)*	*–2.3 (11.5)*	*–0.2 (9.6)*
–5.2 (7.6)	*–1.3 (8.6)*	*0.1 (15.8)*	*3.3 (10.6)*	*1.2 (10.4)*
–3.3 (7.9)	*–4.2 (10.3)*	*–1.9 (8.6)*	*1.4 (10.1)*	*–3.3 (11.1)*
0.6 (7.0)	*–1.8 (9.0)*	*–5.5 (10.4)*	*–5.8 (10.1)*	*0.4 (7.4)*
–3.2 (7.0)	*–1.5 (8.0)*	*–5.4 (9.5)*	*–4.9 (8.1)*	*2.9 (9.4)*

DOI til publisert versjon / DOI to published version: 10.1080/01431160210153039

Table 7 RMS between INSAR DEM and NPI DEM for some baselines

By	*11.0*	*76.0*	*137.0*	*189.5*
RMS	*85.9*	*26.8*	*13.2*	*9.3*

DOI til publisert versjon / DOI to published version: 10.1080/01431160210153039

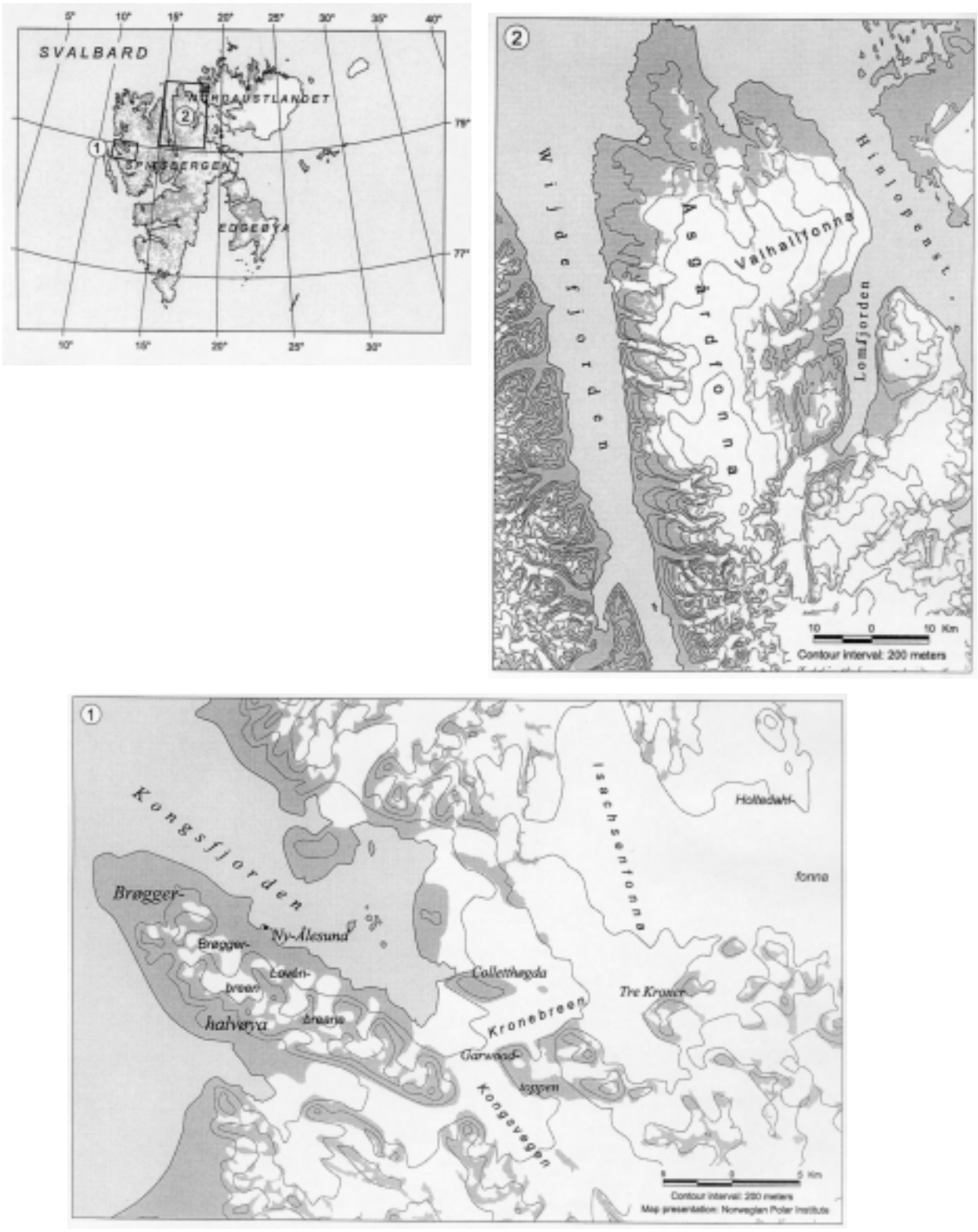

Figure 1

Dette er en postprint-versjon / This is a postprint version.
DOI til publisert versjon / DOI to published version: 10.1080/01431160210153039

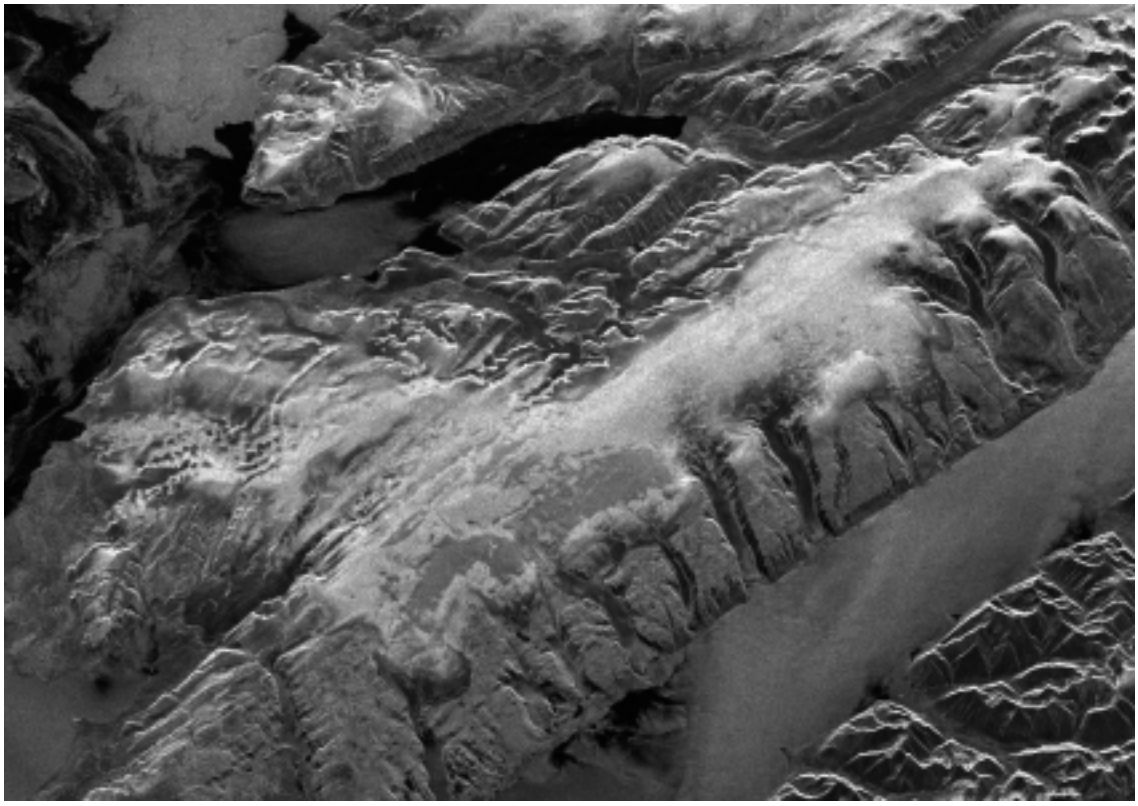

Figure 2

DOI til publisert versjon / DOI to published version: 10.1080/01431160210153039

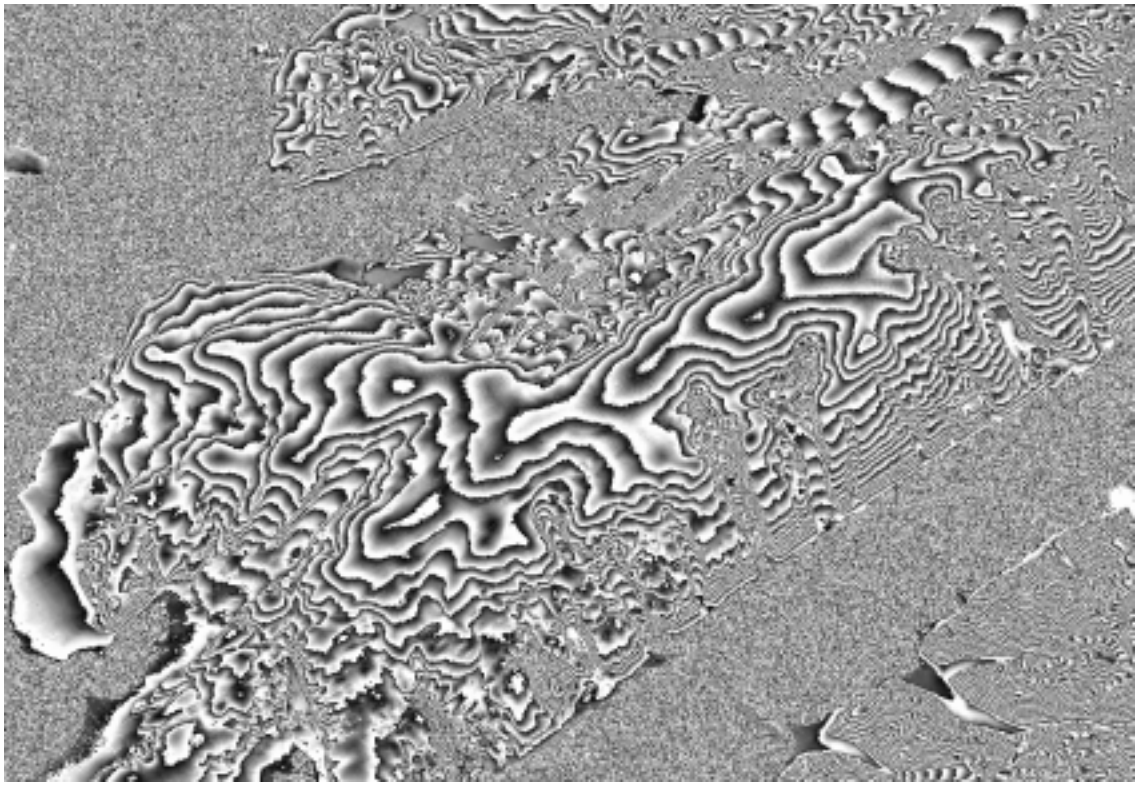

Figure 3

DOI til publisert versjon / DOI to published version: 10.1080/01431160210153039

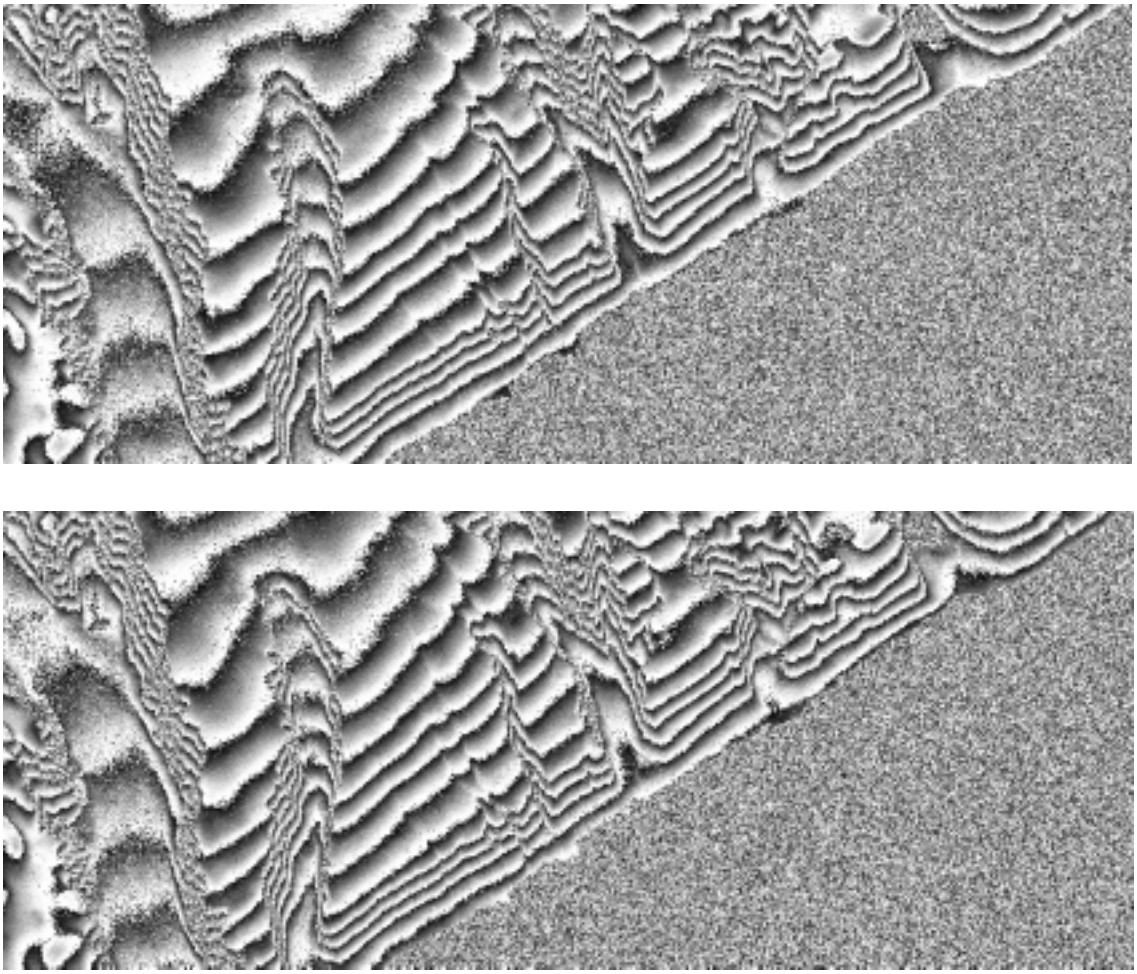

Figure 4

DOI til publisert versjon / DOI to published version: 10.1080/01431160210153039

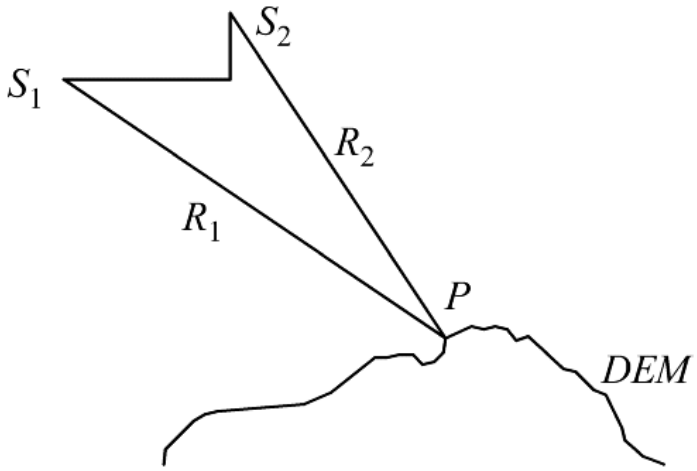

Figure 5

DOI til publisert versjon / DOI to published version: 10.1080/01431160210153039

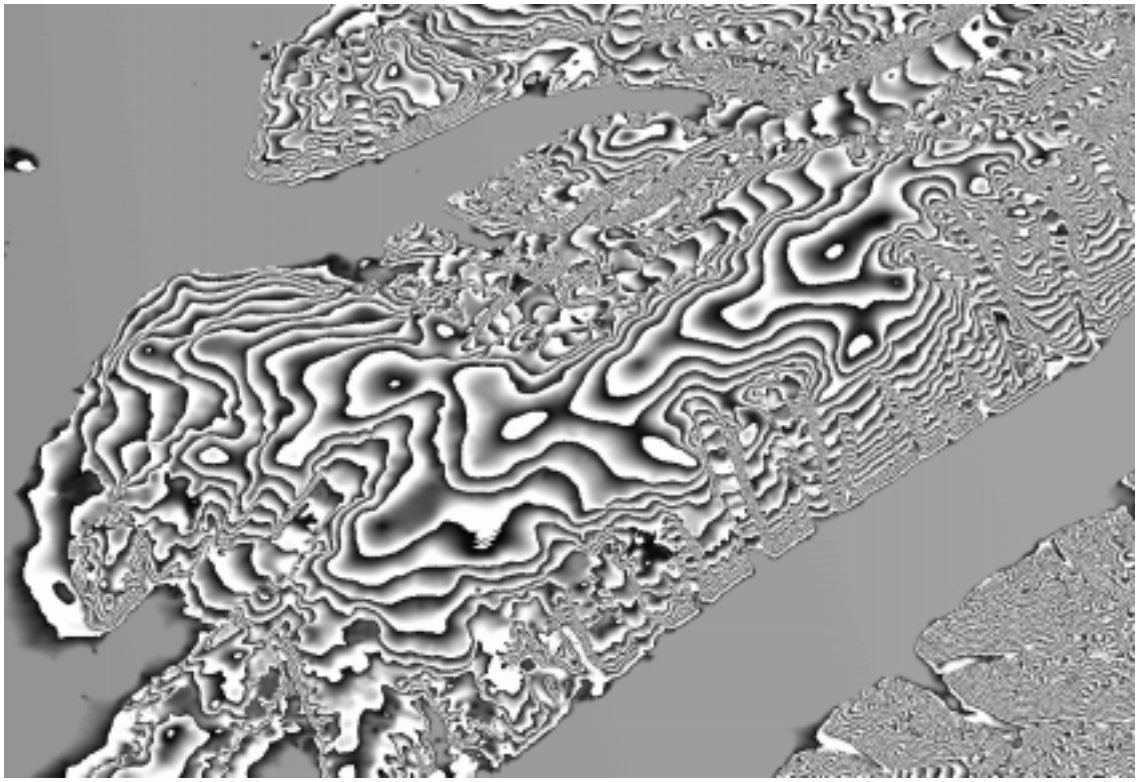

Figure 6

DOI til publisert versjon / DOI to published version: 10.1080/01431160210153039

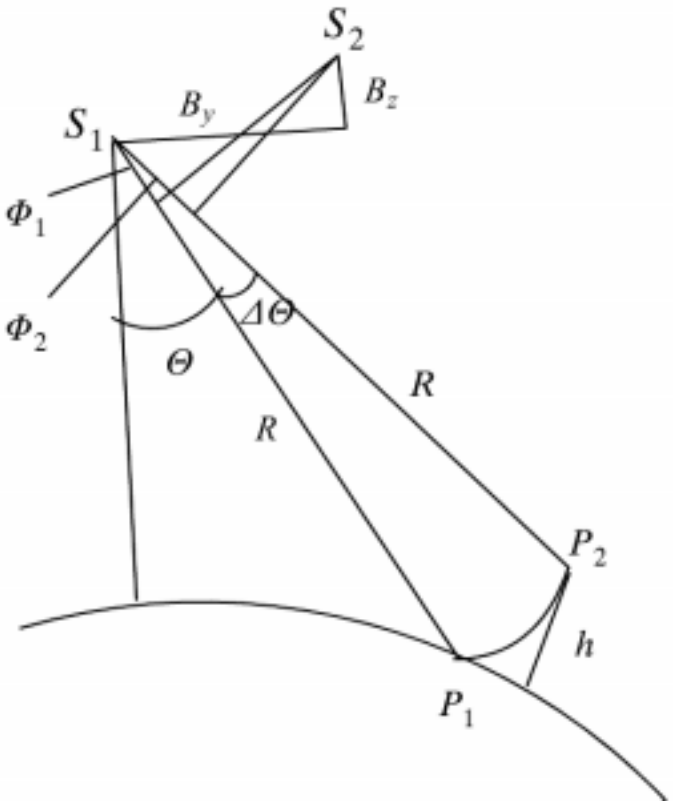

Figure 7

DOI til publisert versjon / DOI to published version: 10.1080/01431160210153039

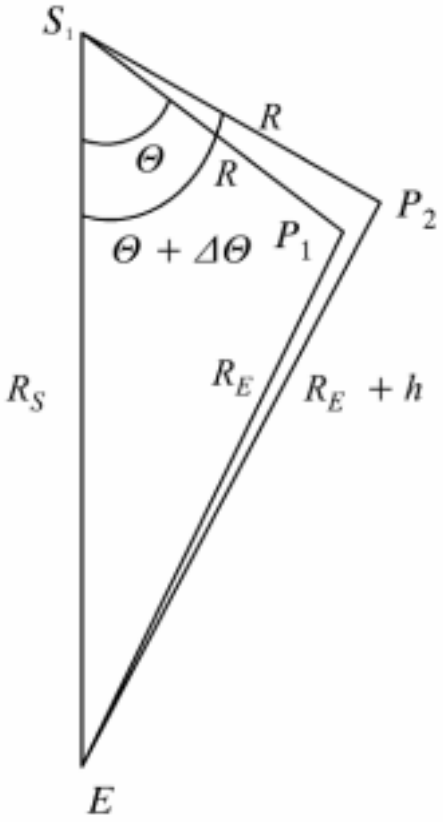

Figure 8

DOI til publisert versjon / DOI to published version: 10.1080/01431160210153039

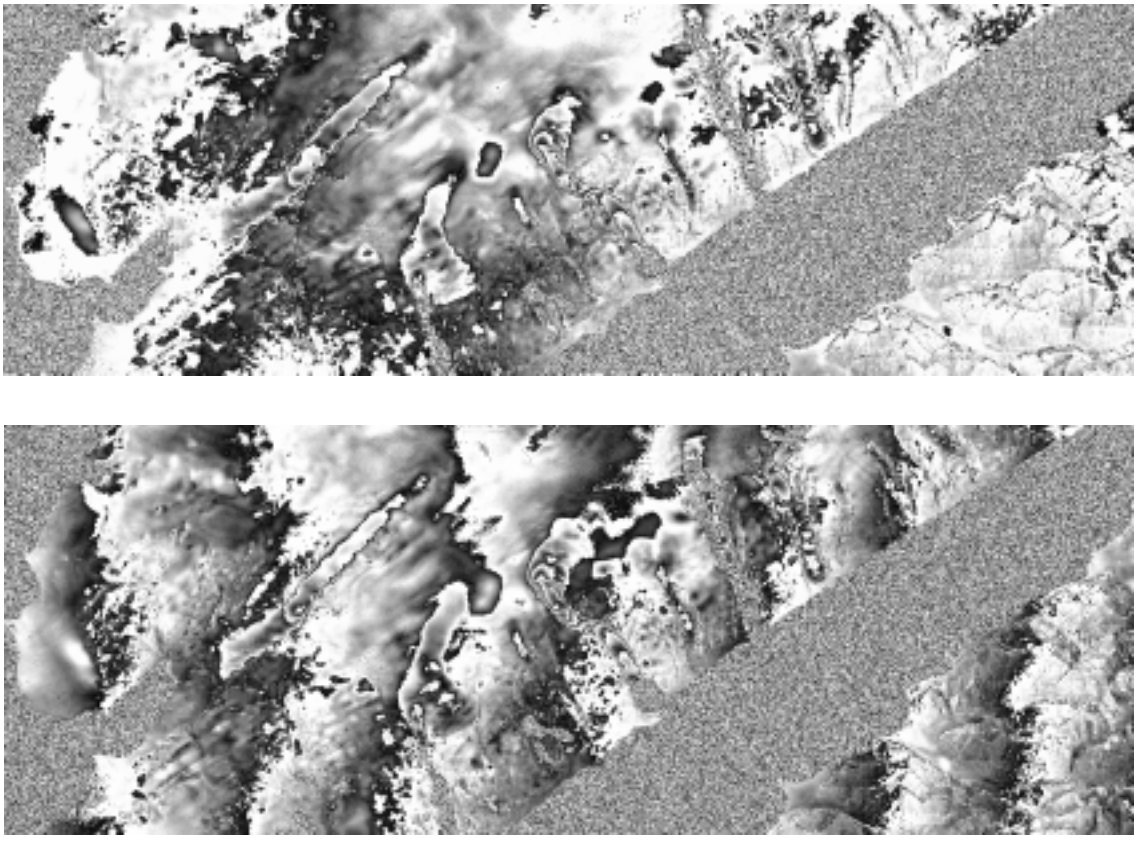

Figure 9

DOI til publisert versjon / DOI to published version: 10.1080/01431160210153039

Figure 10

DOI til publisert versjon / DOI to published version: 10.1080/01431160210153039

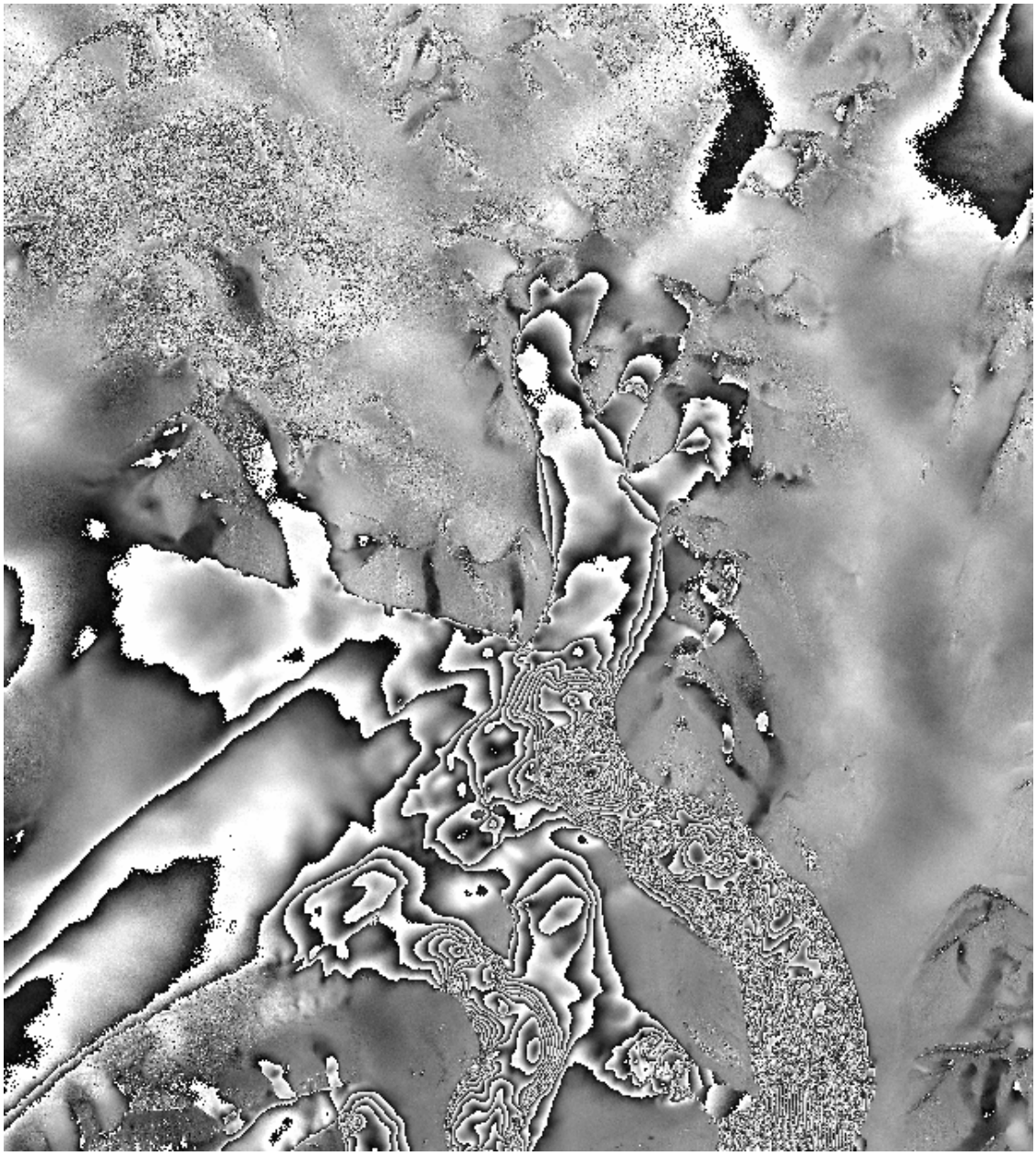

Figure 11

DOI til publisert versjon / DOI to published version: 10.1080/01431160210153039

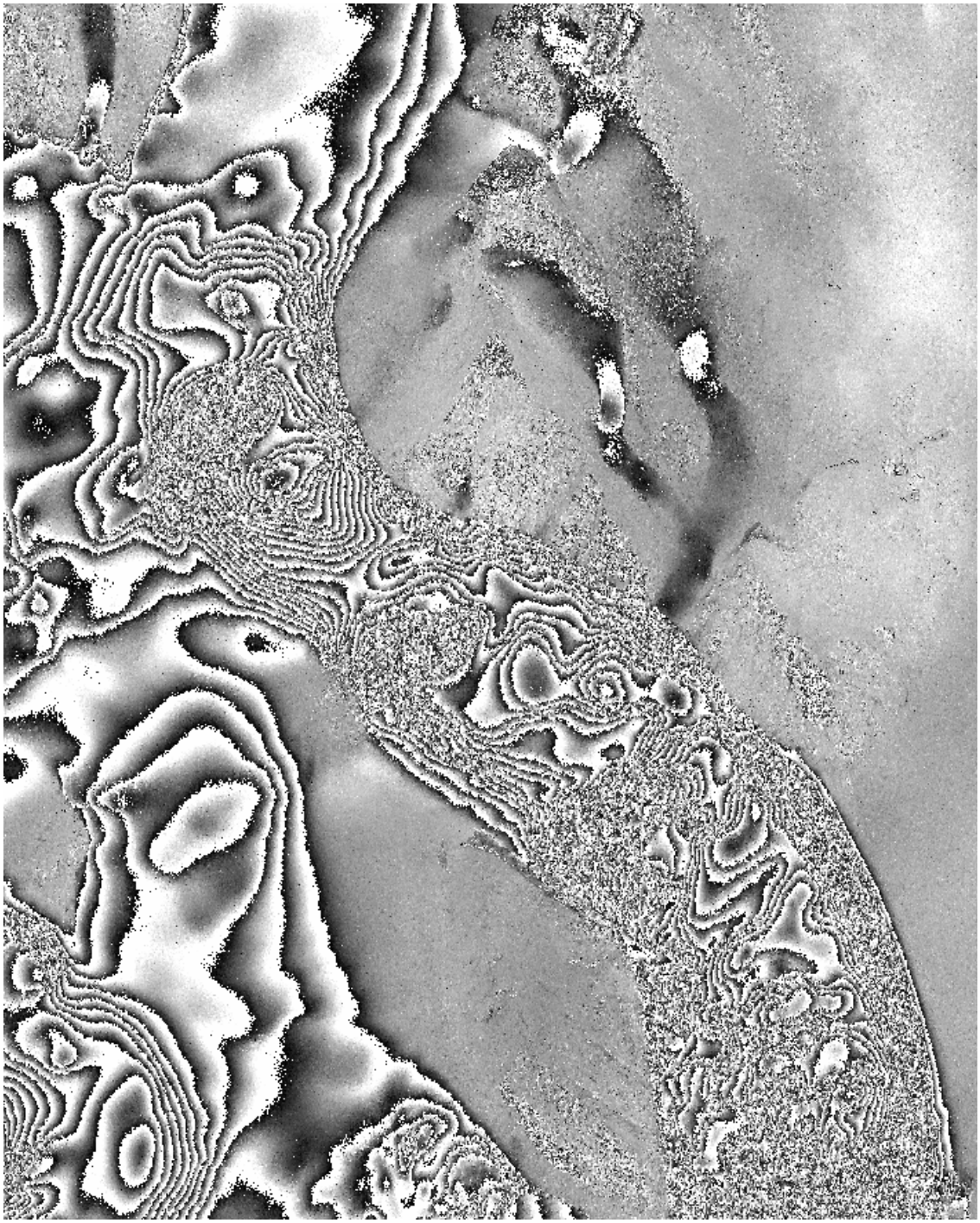

Figure 12

DOI til publisert versjon / DOI to published version: 10.1080/01431160210153039

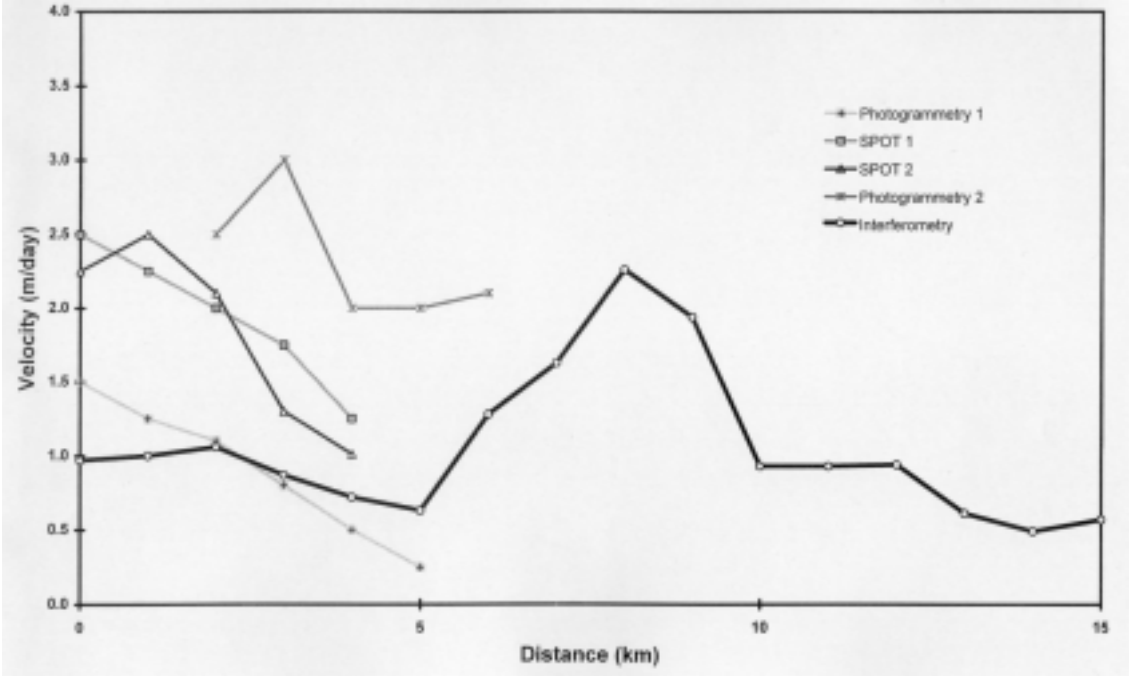

Figure 13

DOI til publisert versjon / DOI to published version: 10.1080/01431160210153039

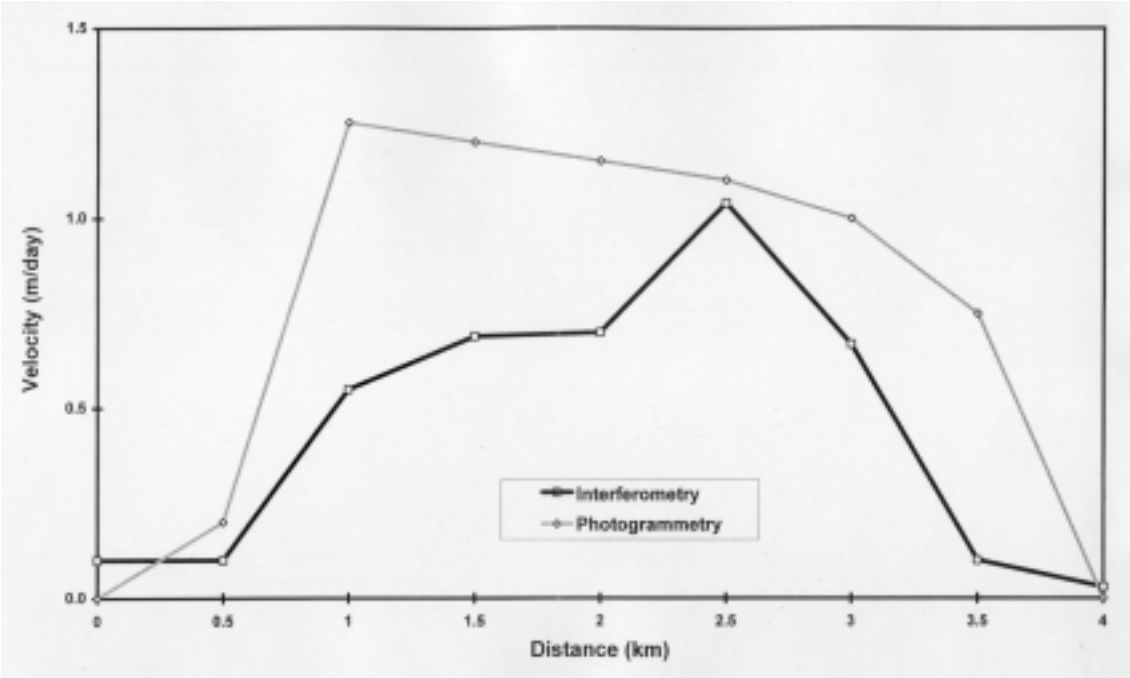

Figure 14

Dette er en postprint-versjon / This is a postprint version.
DOI til publisert versjon / DOI to published version: 10.1080/01431160210153039

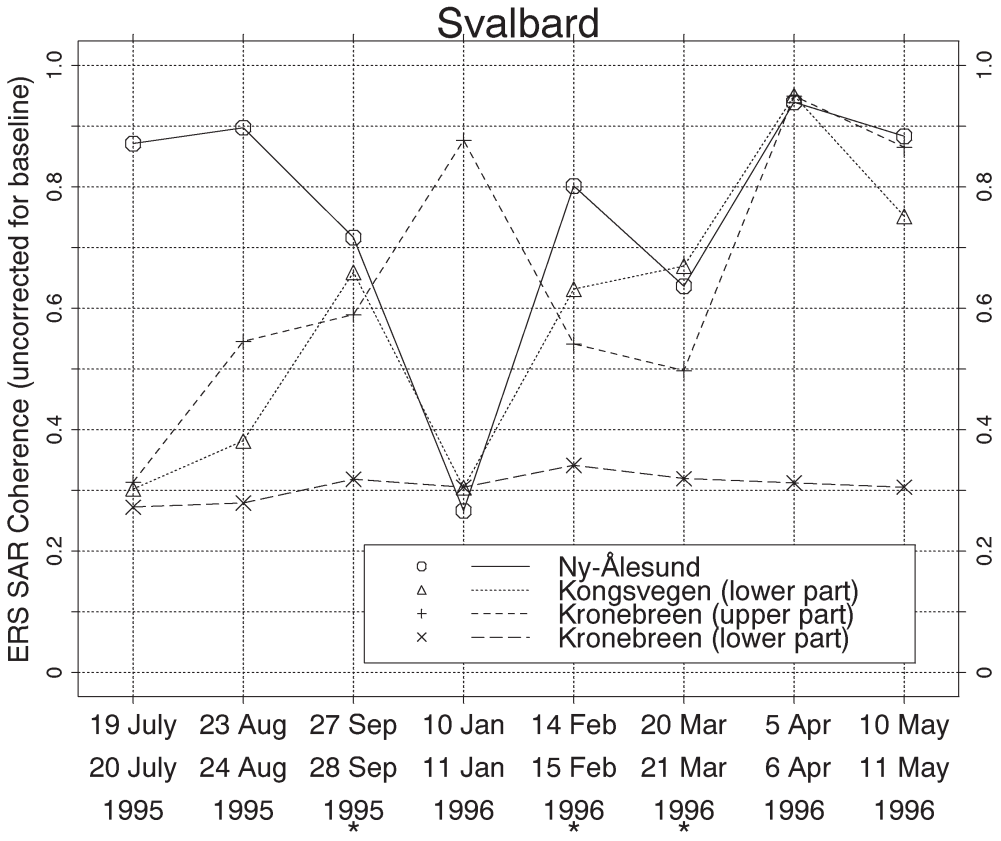

Figure 15

Dette er en postprint-versjon / This is a postprint version.
DOI til publisert versjon / DOI to published version: 10.1080/01431160210153039

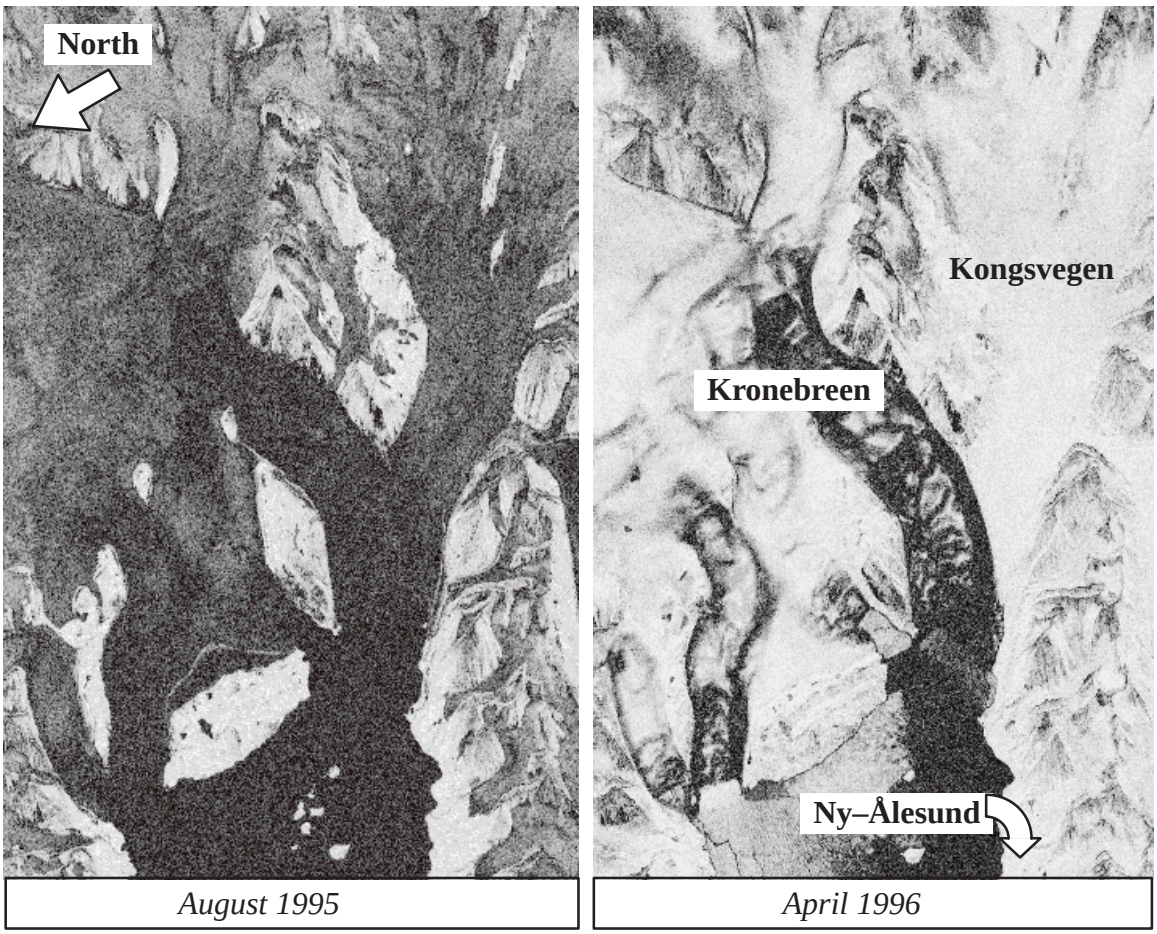

Figure 16

DOI til publisert versjon / DOI to published version: 10.1080/01431160210153039